

Octave-spanning visible supercontinuum generation from an aluminum nitride single crystal pumped by a 355 nm nanosecond pulse

Chunbo Li (李春波)^{1,2,3}, Xikui Ren (任席奎)^{1,2}, Honglei Wu (武红磊)²,
Ruisheng Zheng (郑瑞生)², Junqing Zhao (赵俊清)⁴, Deqin Ouyang (欧阳德钦)³,
Chenlin Du (杜晨林)^{1,2,3}, Peiguang Yan (闫培光)^{1,2}, and Shuangchen Ruan (阮双琛)^{1,2,3,*}

¹Shenzhen Key Laboratory of Laser Engineering, College of Optoelectronic Engineering, Shenzhen University, Shenzhen 518060, China

²Sino-German College for Intelligent Manufacturing, Shenzhen Technology University, Shenzhen 518060, China

³Key Laboratory of Optoelectronic Devices and Systems of Ministry of Education and Guangdong Province, Shenzhen University, Shenzhen 518060, China

⁴Jiangsu Key Laboratory of Advanced Laser Materials and Devices, School of Physics and Electronic Engineering, Jiangsu Normal University, Xuzhou 221116, China

*Corresponding author: scruan@szu.edu.cn

Received November 29, 2017; accepted February 28, 2018; posted online March 28, 2018

Supercontinuum generation (SC) of more than one octave spectrum spanning covering from 400 nm to 820 nm was achieved by pumping a piece of aluminum nitride (AlN) single crystal using a nanosecond 355 nm ultraviolet laser. The AlN with a thickness of ~0.8 mm was grown by an optimized physical vapor transport technique and polished with solidification technology. Compared to previously reported ones, the achieved visible SC exhibited the broadest spectrum spanning from bulk materials pumped by a nanosecond pulse laser. The visible supercontinuum in AlN presents new opportunities for bulk material-based white light SC and may find more potential applications beyond typical applications in integrated semiconductive photoelectronic devices.

OCIS codes: 320.6629, 190.2640, 190.4720, 190.4380.

doi: 10.3788/COL201816.043201.

As a source of coherent broadband light, the supercontinuum (SC) has been studied for more than four decades due to its vast variety of applications, such as spectroscopy, white light microscopy, optical frequency comb, and being a seed source for optical parametric amplification of ultrashort pulses. Many SC sources with a spectrum spanning broader than one octave of bandwidth have been demonstrated by using fibers or bulk solid state samples pumped by femtosecond, picosecond, or nanosecond laser pulses^[1-7]. Several nonlinear optical effects, such as self-phase modulation (SPM), stimulated Raman scattering (SRS), four-wave mixing (FWM), modulation instability (MI), and soliton splitting, typically contribute to the overall propagation dynamics mechanisms for SC generation. The studies on SC generation in the past decades have mostly been explored in fibers, especially in photonic crystals and chalcogenide fibers^[1,8-15]. However, there are intrinsic peak power limitation issues on fiber-based SC generation. The power handling capability of some nonlinear optical bulk materials presents new opportunities for SC generation in the normal and anomalous group velocity dispersion regimes and shows no confinement loss with wavelength^[2,4,5,16-21].

Aluminum nitride (AlN) possesses many fascinating properties, such as high thermal conductivity ($340 \text{ W} \cdot \text{m}^{-1} \cdot \text{K}^{-1}$) and melting point (3546°C), which greatly improve the heat dissipation and thus enhance

the power handling capability. Meanwhile, the low dielectric constant and good mechanical strength are also important characteristics for optical applications^[12-26]. In recent years, tremendous efforts have been devoted to its luminescence properties, including photoluminescence, cathodoluminescence, afterglow luminescence, thermoluminescence, and optically stimulated luminescence^[27-31]. Advantageously, AlN, as a nonlinear optical material with a large nonlinear coefficient, a wide range of transparency, a high optical damage threshold, and good thermal stability, has also gained much attention to its nonlinear properties^[32-34]. Compared to silica ($n_2 = 2.6 \times 10^{-20} \text{ m}^2/\text{W}$), the second-order optical nonlinearity of AlN^[35] [$n_2 = (2.3 \pm 1.5) \times 10^{-19} \text{ m}^2/\text{W}$] is approximately an order larger in magnitude. However, to the best of our knowledge, there are no experimental or theoretical reports on the SC generation based on AlN.

In this Letter, we investigated the visible SC generation in an AlN single crystal and utilized a Raman-enhanced resonant cavity to increase the generation efficiency. The SC can span from 400 nm to 820 nm when pumped by a 355 nm laser pulse with an average power of 9 W. The dominant nonlinear effects, i.e., cascade SRS, Raman-enhanced SPM and cross phase modulation (XPM), facilitate the SC generation.

The AlN growth device is a resistance heating multi-functional single crystal growth furnace with self-refit. The raw AlN powder, with a purity of ~99%, was prepared

by self-propagating combustion of high-purity aluminum powder in a pure nitrogen atmosphere ($\sim 99.999\%$). The particle size was $\sim 0.5 \mu\text{m}$ after grinding. Because of the oxidation of aluminum powder and the surface adsorption of AlN powder, oxygen of $\sim 0.08\%$ is the main impurity material in the AlN powder. Since the high content of oxygen impurity is bound to affect the quality of the AlN single crystal, pre-sintering processes have been adopted to remove the oxygen impurity of the AlN powder. The process of an AlN single crystal includes two steps, i.e., pre-sintering of the AlN powder and crystal growth. In the pre-sintering step, the tungsten crucible with AlN powder is placed into a single crystal growth furnace, vacuumized to $\sim 2 \times 10^{-3} \text{ Pa}$, and heated to $\sim 800^\circ\text{C}$ for 1 h, to remove adsorbed oxygen and water vapor from the crucible and the heat preservation device. Then the furnace is filled with high-purity nitrogen to 1 atm pressure, and the tungsten is heated to $\sim 1900^\circ\text{C}$ for 3 h. Then, by cooling the tungsten down to room temperature, the AlN powder is further purified and sintered since the oxygen aluminum compounds can be sublimated below 1900°C .

In the second step, the sintered AlN is used as the raw material for crystal growth. With a high-nitrogen atmosphere (99.999%) at 1 atm pressure, the components of AlN, i.e., Al and N_2 , can be sublimated from the sintered AlN at the hot bottom of the crucible, which can be re-condensed at the crucible lid where the temperature is relatively lower. In other words, in the crystal growth, the overall reaction $\text{AlN}(\text{s}) \leftrightarrow \text{Al}(\text{g}) + (1/2)\text{N}_2(\text{g})$ runs in the forward (sublimation) direction at the source, and in the reverse (re-condensation) direction at the top of the crucible. The AlN crystal can be formed and grown on top of the crucible lid. The sintered AlN usually begins to sublimate above 1800°C . Achieving high-quality AlN crystals in bulk at a fast growth rate ($>200 \mu\text{m}/\text{h}$) requires a high temperature, above 2100°C . Compared to the first step, the processes of vacuumizing, heating, and filling with high-purity nitrogen are the same with the pre-sintering. The tungsten was heated to 2250°C at 1 atm for 9 h, and then slowly lowered down to room temperature. The AlN single crystal is finally grown on the tungsten sheet with $\sim 10 \text{ mm}$ in size.

When the crystal was removed from the tungsten sheet, one surface of the AlN sample was smooth and the opposite side was rough. The hardness of the AlN crystal is $800 \text{ kg} \cdot \text{mm}^{-2}$ and the size is just $\sim 10 \text{ mm}$, which is too hard and brittle to shape and grind by normal manners. Meanwhile, the AlN single crystal is too small to clamp in the normal fixture. Then acrylic powder and solvent were used to solidify the AlN single crystal with the diameter of a 25 mm grinding sample. Figure 1 shows the solidification processing of the grinding sample. A grinder-polisher (MetaSer 250) was utilized to polish the AlN single crystal. Figure 2 is the polishing schematic. The sample was polished for 5 min with 600 mesh and 1200 mesh SiC-coated abrasive paper, respectively, for the first and second coarse grinding with 20 N pressure force and 150

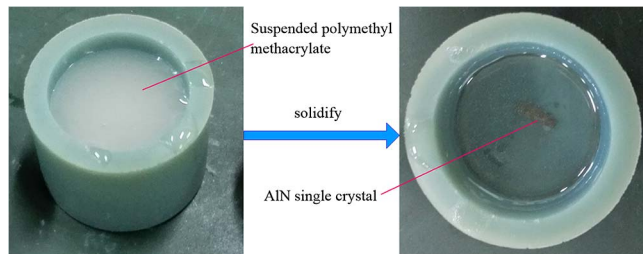


Fig. 1. Solidification process of the grinding sample.

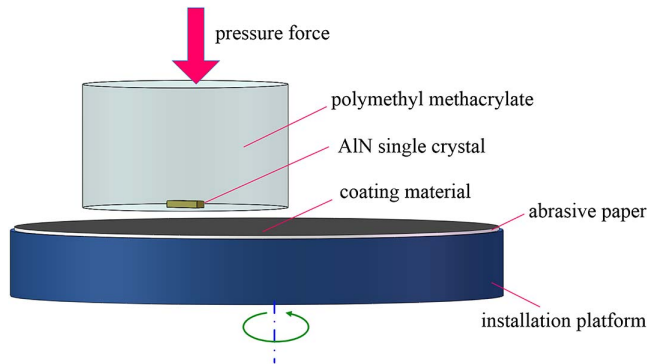


Fig. 2. Schematic illustration of the polishing process.

revolutions per minute (RPM) of the installation platform. Then 6 and $1 \mu\text{m}$ monocrystalline diamond suspensions were used for the third and fourth fine grinding with 10 N pressure force and 120 RPM grinding rotating speed, and the polishing duration was $\sim 20 \text{ min}$. Finally $0.06 \mu\text{m}$ colloidal silica polishing suspension was used for 60 min polishing with 5 N pressure force and 100 RPM grinding rotating speed. Pressure force is a key parameter for polishing the sample at different steps. The larger pressure would lead the AlN single crystal to be cracked or even to be broken during the grinding process. Finally, the polymethyl methacrylate of the ground sample was dissolved with an acetone solution. The polished single crystal was washed using an ultrasonic cleaning machine with an acetone solution for $\sim 60 \text{ min}$ to relieve the stress and clean the residual polymethacrylate. The opposite face was polished with the same procedure.

We used X-ray diffraction (XRD) measurement to evaluate the crystal quality. Figure 3 shows the sample's $\omega/(2\theta)$ XRD data, with only a sharp diffraction peak for wurtzite (100), indicating that the AlN crystal's growth is only surface-oriented in the M plane. The AlN crystal exhibits a maximum length of $\sim 10 \text{ mm}$, as shown in the inset of Fig. 3.

The Raman spectrum of the polished AlN single crystal was measured using a Horiba Jobin-Yvon LabRam HR800 system with a nitrogen-cooled charge-coupled-device (CCD) camera. The 325 nm line of a He-Cd laser was used as the excitation source. The spectral resolution was $\sim 1 \text{ cm}^{-1}$, and the laser power was $\sim 15 \text{ mW}$. Figure 4 shows the Raman spectrum of the polished AlN under

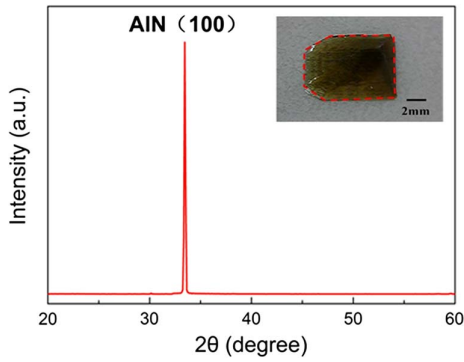


Fig. 3. XRD spectrum of the as-obtained AlN crystal. Inset: photograph of the polished AlN single crystal.

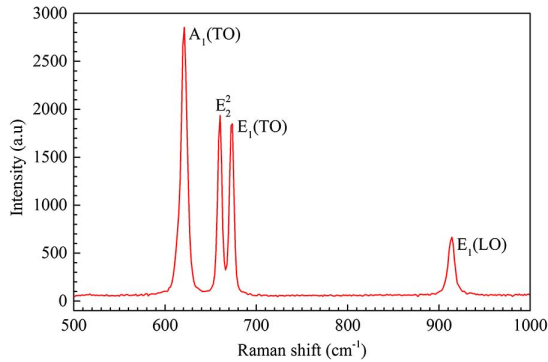


Fig. 4. Raman spectrum of the polished AlN under ambient conditions.

normal pressure and room temperature. Raman-active optical phonon modes of $A_1(\text{TO})$, E_2^2 , $E_1(\text{TO})$, and $E_1(\text{LO})$ can be clearly observed from the Raman spectrum. The peak positions of the four modes are centered at 620.96, 660.18, 673.77, and 914.12 cm^{-1} , respectively, which agree well with other reports^[36].

Figure 5 presents the experimental setup for the SC generation. The UV laser at 355 nm is a diode-pumped third harmonic Q -switched solid-state laser that can deliver UV pulses with a maximum average power of ~ 9 W and maximum peak power of ~ 50 kW, respectively. A spectrometer

(Avantes 4368) with a Si photodetector is used for the spectrum measurement. The laser pulse can be focused into the AlN single crystal with a peak intensity of $\sim 10^{12}$ W/cm^2 (spot size of 22.2 μm). Prior to the focusing lens, a narrow bandpass filter is inserted to block the unconverted second harmonic and fundamental laser beams at 532 and 1064 nm, respectively. L1 is a UV-fused silica plano-convex lens with a focusing length of 100 mm. Then two dichroic mirrors (DMs), with a transmittance higher than 80% at 330–360 nm and a reflectivity higher than 95% at 385–450 nm, were used to construct a Raman resonant enhanced cavity. Afterward, L2 with a focusing length of 50 mm was used to collect the generated light from the AlN sample, and a longpass filter was used to block the 355 nm pump light. L1, L2, and the AlN can be moved forward and backward to obtain the best positions to produce and collect the visible SC. A spectrometer (AvaSpec-ULS3648) with a slit size of 10 μm and a resolution of 0.05–0.06 nm was utilized to measure the generated SC spectra.

Figure 6 shows the spectra of the SC with different pump powers. The SC exhibits a red frequency shift as the single-pulse energy increases. The experimental results indicate that the spectral broadening of the SC is impressively extended. It shows a wide and flat spectral profile in the range from 400 nm to 465 nm, and seven remarkable peaks at 471, 495, 519, 553, 593, 626, and 659 nm, respectively, with a pump power of 8 W or 9 W. The threshold average pump power for the SC generation is ~ 3 W with spectrum broadening from 400 nm to 557 nm. Four small peaks can be found on the spectrum profile under a pump power of 7 W, which increases to seven with ~ 8 W or ~ 9 W pump powers. These indicate that 7 W is approximately the threshold power of higher-order SRS initiation.

Figure 7 shows the SC generation from the AlN single crystal at a pump power of 9 W with a logarithmic scale, and the inset shows the corresponding output far-field beam profile. The maximum intensity difference of the flat spectrum spanning from 400 nm to 653 nm is ~ 5 dB. The whole spectrum is spanning from 400 nm to 820 nm. From Fig. 7, it can also be clearly seen that the spectrum width

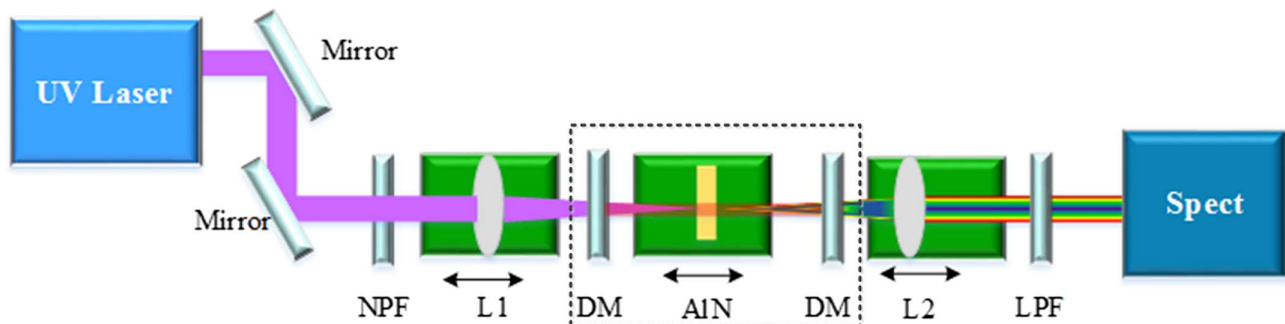


Fig. 5. Experimental setup for the SC generation. UV laser: 355 nm laser; Mirror: flat mirror with protected aluminum; NPF: narrow-bandpass filter; L1, L2: UV-fused silica plano-convex lenses; DM: dichroic mirrors HT@330–360 nm and HR@385–450 nm; LPF: longpass filter; Spect: spectrometer.

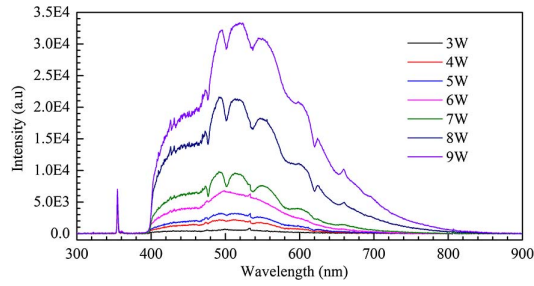


Fig. 6. Supercontinuum evolution with different pump powers at 355 nm.

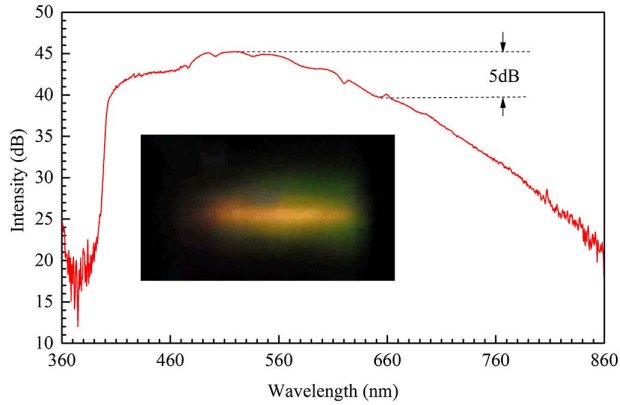


Fig. 7. Output spectrum at the maximum pump power of 9 W. Inset: the corresponding output far-field beam profile.

and intensity of the SC linearly increase with the pump power. At ~ 9 W average power emission, the corresponding pulse duration is ~ 30 ns with a peak power of ~ 50 kW.

Figure 8 gives the relationship between the output characteristics and the input pump power. The broadened spectrum and output power show an almost linear increase with the input pump power. The generated maximum output power and corresponding slope efficiency are 1.6 W and $\sim 27\%$, respectively. It should be noted that 9 W is not the saturated input pump power for the SC

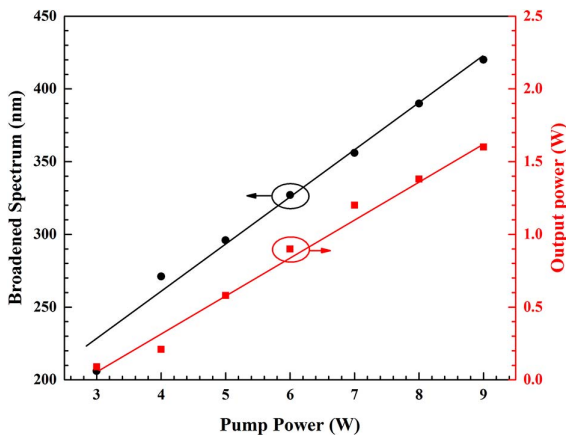


Fig. 8. Relationship between the output characteristics and the input pump power.

generation, and the spectrum should be broader with a larger pump power, although our pump laser is currently limited to ~ 9 W.

Many nonlinear mechanisms should contribute to the achieved SC spectral broadening. The zero-dispersion wavelength (ZDW) of the AlN single-crystal is $\sim 1.6 \mu\text{m}$ ^[30]. For a normal dispersion pumping regime, the 355 nm pumping light is far from the ZDW of the AlN, and SPM is responsible for the initial spectral broadening. The intensive nonlinear effect of SPM causes a refractive index change when the strong optical pulse propagates through the AlN single crystal. Nonlinear phase change is an important parameter for characterizing the nonlinear progress. The well-known formula to calculate the nonlinear phase is $\psi_{\text{NL}} = \gamma P_0 L_{\text{eff}}$, where γ is the nonlinear coefficient of the polished AlN single crystal, $P_0 = \sim 50$ kW is the maximum pulse peak power at 355 nm, and L_{eff} is the effective length of the polished AlN single crystal in the propagating fiber. The nonlinear coefficient $\gamma = 2\pi n_2 / \lambda A_{\text{eff}}$, where n_2 is the second-order optical nonlinearity coefficient. For AlN, the n_2 is typically around $2.3 \times 10^{-19} \text{ m}^2/\text{W}$, and A_{eff} is the effective area. L_{eff} is the effective length, which approximately equals the AlN thickness of 0.8 mm. According to these relationships, we can calculate that, with the maximum pulse peak power, the nonlinear phase change is ~ 0.4 rad for a pulse single pass through the crystal. Meanwhile, SRS effects have also been observed in our experiment, which is an important process that competes with SPM. The Raman-induced frequency shift is responsible for the long-wavelength components of the SC^[37]. The theoretical research has been explored by Gerston *et al.* to describe the resonance enhancement of χ^3 , and cross modulation and interference between the SRS and SPM. The Stokes pulse broadens due to a combination of XPM and Raman parametric amplification^[38].

In a wurtzite AlN crystal, there are six optical phonon modes of $1A_1$, $2B_1$, $1E_1$, and $2E_2$ in the center of the Brillouin zone, and the A_1 and E_1 modes are Raman- and infrared-active, where A_1 is polarized along the z direction and E_1 is polarized in the x - y plane. The E_2 mode, being twofold degenerate, is only Raman-active^[35]. The two B_1 modes are silent modes. At room temperature, the Raman shift of four Raman-active optical phonon modes of $A_1(\text{TO})$, E_2^2 , and $E_1(\text{LO})$ are 620.96, 660.18, 673.77, and 914.12 cm^{-1} , respectively. Most of the low-order stimulated Raman scattering of the optical phonon modes are in the spectrum of 385–450 nm. In the case of SRS, the frequency shift takes place in units of the vibrational frequencies of the single crystal molecular AlN in a quantized manner for the energy transferring from the primary mode of the laser frequency to other modes. The main mode becomes depleted and the Stokes modes are intensified. The Stokes mode occurs in a quantized manner when the SC occurs. However, the spectrum of SPM is broadening in a gradual manner. When the laser pulses pass through the single crystal AlN, owing to the nonlinearity and the Raman-enhanced cavity, the pulse and

Stokes light oscillate against each other and gradually broaden the SC spectrum.

Meanwhile, under ~ 8 W or ~ 9 W of pump power, the six strong peaks observed on the spectral profile (Fig. 6) indicate that a Raman bullet is radiated resulting from the molecular response and interaction with each other. These Stokes components satisfy the energy conservation condition of FWM as $2\omega_{495\text{ nm}} = \omega_{571\text{ nm}} + \omega_{519\text{ nm}}$ and $2\omega_{626\text{ nm}} = \omega_{593\text{ nm}} + \omega_{659\text{ nm}}$.

In conclusion, we have demonstrated the octave-spanning visible SC generation from an AlN single crystal with 355 nm UV laser pumping assisted with a Raman-enhanced-cavity configuration. The main nonlinear processes contributing to the SC generation are cascade SRS, Raman-enhanced SPM, XPM, and FWM. To the best of our knowledge, it is the broadest visible SC in bulk material with nanosecond pulse pumping. This Raman-enhanced resonant cavity may also provide a useful configuration to enhance the broadband SC generation in bulk materials.

This work was supported by the National Natural Science Foundation of China (NSFC) (Nos. 61575129 and 11447029) and the Science & Technology Innovation Committee Foundation of Shenzhen (No. JCYJ20160328144942069).

References

1. X. Jiang, N. Joly, M. Finger, F. Babic, G. Wong, J. Travers, and P. Russell, *Nat. Photon.* **9**, 133 (2015).
2. F. Silva, D. Austin, A. Thai, M. Baudisch, M. Hemmer, D. Faccio, A. Couairon, and J. Biegert, *Nat. Commun.* **3**, 807 (2012).
3. C. Petersen, U. Møller, I. Kubat, B. Zhou, S. Dupont, J. Ramsay, T. Benson, S. Sujecki, N. Abdel-Moneim, Z. Tang, D. Furniss, A. Seddon, and O. Bang, *Nat. Photon.* **8**, 830 (2014).
4. H. Liang, P. Krogen, R. Grynko, O. Novak, C. Chang, G. Stein, D. Weerawarne, B. Shim, F. Kartner, and K. Hong, *Opt. Lett.* **40**, 1069 (2015).
5. A. Lanin, A. Voronin, E. Stepanov, A. Fedotov, and A. Zheltikov, *Opt. Lett.* **40**, 974 (2015).
6. S. Vyas, T. Tanabe, M. Tiwari, and G. Singh, *Chin. Opt. Lett.* **14**, 123201 (2016).
7. M. Klimczak, B. Siwicki, A. Heidt, and R. Buczynsk, *Photon. Res.* **5**, 710 (2017).
8. E. Serebryannikov and A. Zheltikov, *Opt. Commun.* **274**, 433 (2007).
9. J. Dudley, G. Genty, and S. Coen, *Rev. Mod. Phys.* **78**, 1135 (2006).
10. S. Coen, A. Chau, R. Leonhardt, J. Harvey, J. Knight, W. Wadsworth, and P. Russell, *J. Opt. Soc. Am. B* **19**, 753 (2002).
11. P. Yan, J. Shu, S. Ruan, J. Zhao, J. Zhao, C. Du, C. Guo, H. Wei, and J. Luo, *Opt. Express* **19**, 4985 (2011).
12. S. Coen, A. Chau, R. Leonhardt, J. Harvey, J. Knight, W. Wadsworth, and P. Russell, *Opt. Lett.* **26**, 1356 (2001).
13. B. Yan, J. Yuan, X. Sang, K. Wang, and C. Yu, *Chin. Opt. Lett.* **14**, 050603 (2016).
14. Z. Zheng, D. Ouyang, J. Zhao, M. Liu, S. Ruan, P. Yan, and J. Wang, *Photon. Res.* **4**, 135 (2016).
15. P. S. Maji and R. Das, *Chin. Opt. Lett.* **15**, 070606 (2017).
16. J. Dharmadhikari, R. Deshpande, A. Nath, K. Dota, D. Mathur, and A. Dharmadhikari, *Appl. Phys. B* **117**, 471 (2014).
17. C. Lu, L. Yang, M. Zhi, A. Sokolov, S. Yang, C. Hsu, and A. Kung, *Opt. Express* **22**, 4075 (2014).
18. T. Cheng, L. Zhang, X. Xue, D. Deng, T. Suzuki, and Y. Ohishi, *Opt. Express* **23**, 4125 (2015).
19. B. Zhou, H. Guo, and M. Bache, *Opt. Express* **23**, 6924 (2015).
20. M. Hemmer, M. Baudisch, A. Thai, A. Couairon, and J. Biegert, *Opt. Express* **21**, 28095 (2013).
21. T. Kardaś, B. Ratajska-Gadomska, W. Gadomski, A. Lapini, and R. Righini, *Opt. Express* **21**, 24201 (2013).
22. H. Rinnert, S. Hussain, V. Brien, J. Legrand, and P. Pigeat, *J. Lumin.* **132**, 2367 (2012).
23. M. Soares, J. Leitão, M. Silva, J. González, F. Matinaga, K. Lorenz, E. Alves, M. Peres, and T. Monteiro, *Opt. Mater.* **33**, 1055 (2011).
24. C. Rodrigues, Á. Vasconcelos, and R. Luzzi, *Eur. Phys. J. B* **72**, 67 (2009).
25. S. Bakalov, A. Szekeres, S. Grigorescu, E. Axente, G. Socol, and I. Mihalescu, *Appl. Phys. A* **85**, 99 (2006).
26. V. Darakhchieva, P. Paskov, M. Schubert, T. Paskova, B. Monemar, S. Kamiyama, M. Iwaya, H. Amano, and I. Akasaki, *Phys. Status Solidi C* **7**, 2614 (2003).
27. Y. Cho, B. Dierre, N. Fukata, N. Hirosaki, K. Marumoto, D. Son, K. Takahashi, T. Takeda, and T. Sekiguchi, *Scr. Mater.* **110**, 109 (2016).
28. S. Inoue, T. Naoki, T. Kinoshita, T. Obata, and H. Yanagi, *Appl. Phys. Lett.* **106**, 131104 (2015).
29. L. Trinkler and B. Berzina, *Phys. Status Solidi B* **251**, 542 (2014).
30. A. Vokhmintsev, I. Weinstein, and D. M. Spiridonov, *J. Lumin.* **132**, 2109 (2012).
31. T. Schulz, M. Albrecht, K. Irmscher, C. Hartmann, J. Wollweber, and R. Fornari, *Phys. Status Solidi B* **248**, 1513 (2011).
32. L. Bergman and J. McHale, *Handbook of Luminescent Semiconductor Materials* (CRC Press, 2012), Chap. 2.
33. W. Pernice, C. Xiong, C. Schuck, and H. Tang, *Appl. Phys. Lett.* **100**, 223501 (2012).
34. M. Larciprete, A. Bosco, A. Belardini, R. Voti, G. Leahu, C. Sibilia, E. Fazio, R. Ostuni, M. Bertolotti, A. Passaseo, B. Poti, and Z. Prete, *J. Appl. Phys.* **100**, 023507 (2006).
35. H. Jung, C. Xiong, K. Fong, X. Zhang, and H. Tang, *Opt. Lett.* **38**, 2810 (2013).
36. M. Kuballa, J. Hayesa, Y. Shi, J. Edgarb, A. Prinsc, N. Udenc, and D. Dunstan, *J. Cryst. Growth* **231**, 391 (2001).
37. J. Swiderski, *Prog. Quantum Electron.* **38**, 189 (2014).
38. J. Gersten, R. Alfano, and M. Belic, *Phys. Rev. A* **21**, 1222 (1980).